# Intercrystal Scatter Rejection for Pixelated PET Detectors

Christian Ritzer, Patrick Hallen, David Schug, and Volkmar Schulz

***Abstract*— High-resolution positron emission tomography (PET) scanners often use pixelated scintillator arrays with lightsharing for the detection of gamma rays. The aim of this paper is to enhance the spatial resolution of such a pixelated scintillator detector by filtering out events with multiple interactions of gamma rays in the scintillator based on the measured light distributions. To develop and evaluate such enhancements in spatial resolution, we measure the point spread function (PSF) of our detector directly using a thinly collimated gamma ray beam setup, and then later verify their benefits on a full preclinical PET system with a hotrod phantom. The scintillator detector comprises a 30 × 30 × 12 $mm^3$ lutetium–yttrium oxyorthosilicate array with a pitch of 1 mm coupled to a digital silicon photomultiplier array via a 2-mm lightguide. We use a center of gravity algorithm for the crystal identification; however, the proposed filters are independent of the crystal identification algorithm. Investigating a single detector with our collimated gamma beam, we reject 15% of the events as multiple interaction while improving the crystal identification efficiency from 60.0% to 68.3% and the 90th-percentile diameter of the PSF from 7.88 to 3.98 mm. On system level, we analyze a line profile through two different rod sizes in a hotrod phantom. The filters reject 32% of the coincidences and increase the peak-to-valley ratio by 8% (0.9-mm rods) and by 18% (1.2-mm rods).**

***Index Terms*— Biomedical imaging, Filtering algorithms, Image enhancement, Positron emission tomography, Spatial resolution.**

## I. Introduction

POSITRON emission tomography (PET) is a functional imaging modality with high sensitivity. It acquires images by detecting the annihilation radiation of positrons. Therefore, the detectors inside a PET system need to detect gamma rays with an energy of 511 keV. One important performance parameters of PET systems is the spatial resolution. Especially, small-animal PET systems require a very high spatial resolution to resolve anatomical features in mice and rats.

Manuscript received August 15, 2016; revised November 11, 2016; accepted December 22, 2016. Date of publication February 6, 2017; date of current version March 24, 2017. This work was supported by the European Community Seventh Framework Program, project no. 241711: SUB nanosecond leverage in PET/MR Imaging (SUBLIMA); the project 'ForSaTum', co-funded by the European Union (European Regional Development Fund – Investing in your future) and the German federal state North Rhine–Westphalia (NRW); Philips Research Europe, Aachen, Germany; and the European Union's Horizon 2020 research and innovation program under Grant Agreement 667211. *(Corresponding authors: Christian Ritzer; Patrick Hallen.) (Christian Ritzer and Patrick Hallen contributed equally to this work.)*

C. Ritzer is with the Department of Physics of Molecular Imaging Systems, Institute for Experimental Molecular Imaging, RWTH Aachen University, 52062 Aachen, Germany, and also with the Institute for Particle Physics, ETH Zürich, 8092 Zürich, Switzerland.

P. Hallen, D. Schug, and V. Schulz are with the Department of Physics of Molecular Imaging Systems, Institute for Experimental Molecular Imaging, RWTH Aachen University, 52062 Aachen, Germany.

Color versions of one or more of the figures in this paper are available online at http://ieeexplore.ieee.org.

Digital Object Identifier 10.1109/TNS.2017.2664921

TABLE I
DIFFERENT EVENT TYPES WITH THE NUMBER OF DETECTOR INTERACTIONS AND THE DEPOSITED ENERGY

| Interaction | # interactions | Deposited energy |
|---|---|---|
| Photo absorption | 1 | 511 keV |
| Scattering + escape | 1 | $<$ 511 keV |
| Multiple scattering + absorption | $>$ 1 | 511 keV |
| Multiple scattering + escape | $>$ 1 | $<$ 511 keV |

Intrinsically, the spatial resolution is limited by the positron range [1] and by the noncollinearity of the annihilation photons [2]. In addition to these physical limits defined by the isotope and the system diameter, the spatial resolution of the gamma detectors itself limits the system resolution.

In this paper, we focus on detectors with pixelated scintillators. The most straightforward way to improve their resolution is to reduce the pitch size of the crystals [3]. If each scintillator pixel is read out individually by a photodetector pixel (one-to-one coupling), smaller crystal sizes will require more readout channels, thus increasing the cost and complexity of the photodetectors and the data acquisition. An alternative approach is to spread the scintillation light over a number of photodetector pixels, allowing the usage of fewer readout channels than crystals ($n$-to-one coupling). This detector geometry is widely used in commercial scanners as well as research detectors such as the Hyperion $II^D$ PET/MR insert, built in our group [4]–[7].

The Compton effect causes scattering of the gamma rays in both the patient (object scattering) and the detector (detector scattering). However, in preclinical PET applications with mice, scatter predominantly occurs in the detector and not in the body of the mouse due to its relative small size [8]. The Hyperion $II^D$ PET/MR insert comprises a lutetium–yttrium oxyorthosilicate (LYSO) scintillator, which has a photofraction of about 33% for 511-keV photons [9]. Therefore, about two-thirds of the gamma ray interactions in our detector material are Compton scattering, which either deposit only a fraction of their energy or interact multiple times.

If these multiple interactions occur in different crystal elements (so-called intercrystal scatter ICS), the resulting light distributions of the interactions will overlap, due to the light sharing. So far, state-of-the-art algorithms for crystal identification are not able to reliably identify the crystal with which the initial gamma ray interacted, thus resulting in a positioning error of the single and subsequently of the corresponding line of response, too. Simulations suggest that this error leads to image blurring and a loss in contrast on system level [10], [11].

The different types of singles can be classified into four categories based on the number of interactions with the

scintillator and the deposited amount of energy in the scintillator. These categories are introduced in Table I. Events with only a single gamma interaction in the scintillator can be positioned correctly, so ideally we want a pure data sample of these events for image reconstruction with the highest spatial resolution. However, it is not possible to simply select these events with an energy cut, because this would reject both single and multiple scatters with subsequent escape but not multiple scatters with full absorption.

In this paper, we present two filters that differentiate single interaction events from multiple-interaction events using only the shape of their light distribution. This can be combined with a large energy window to maintain a high sensitivity. Simulation studies for comparable detector geometries suggest that such filters should be able to improve the image quality significantly [12], [13]. Existing approaches for intercrystal scatter rejection based on maximum likelihood algorithms [14] are much more complicated and entail high computational costs and are therefore very challenging to implement directly in the FPGA of the detector stack. Our filters, on the other hand, are very simple and can easily be implemented in the FPGA or even into a fully analog signal processing chain.

Usually, the performance of the crystal identification is evaluated using so-called floodmap histograms of the light pattern's center of gravity positions and evaluation of the peak-to-valley (PtV) ratios. While this approach may be easy, it does not allow the quantification of the probabilities to identify the correct crystal. To measure the spatial resolution of pixelated scintillation detectors with high precision, we developed a collimator setup that can irradiate single crystals of our scintillator array. This allows us to directly measure the crystal identification efficiency (CIE) and how this can be improved by rejecting ICS events. With this knowledge, we will optimize the filter algorithms and apply them on system level to show their benefits.

This collimator setup closely follows the approach that is used to calibrate and evaluate monolithic scintillators, which are increasingly considered as an alternative to conventional pixelated scintillators [15], [16]. The spatial resolution of monolithic detectors is usually reported as the point spread function (PSF), which is the probability distribution of the error between the measured interaction position and true interaction position. Using our collimated gamma ray beam, we can directly measure the 2-D PSF of our pixelated scintillator detector and compare it with monolithic detectors.

## II. Materials

We use two different setups for this paper: a collimator setup, based on the technology evaluation kit (TEK) from Philips Digital Photon Counting (PDPC), with two scintillation detectors, and the Hyperion-II$^D$ PET scanner, developed by our group, to analyze our filter techniques on system level. Both experiments are equipped with the same scintillator arrays and DPC 3200 digital photodetectors.

### A. Detector Stack

Our gamma ray detectors use pixelated LYSO scintillators to convert the incident gamma rays into visible light.

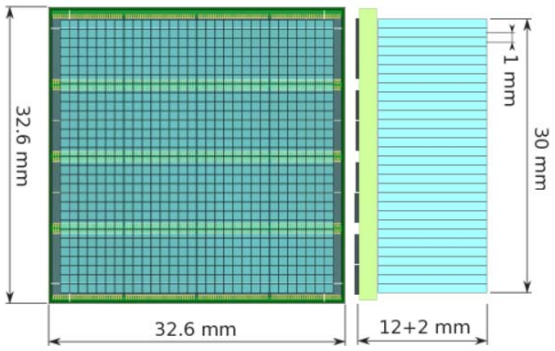


Fig. 1. Sketch of the detector stack (adapted from [17]).

TABLE II
Operation Parameters of the Photodetector

| | |
|---|---|
| Trigger setting | 3 (⌀ 3 photons) |
| Validation setting, collimator | 0x55 (⌀ 15.9 photons) |
| Validation setting, scanner | 0x54 (⌀ 27.5 photons) |
| Overvoltage | 2.5 V |
| Validation time | 40 ns |
| Integration time | 165 ns |

Each scintillator array measures $30 \times 30 \times 12$ mm$^3$ with a pitch of 1 mm. The single crystals are $0.933 \times 0.933$ mm$^2$ in size and are separated by a 67-$\mu$m-thick Vikuity ESR film (3M, St. Paul, USA). The array is glued with a dual-component silicon glue (Scionix, Utrecht, the Netherlands) to a 2-mm-thick borosilicate glass light guide with a size of $32 \times 32$ mm$^2$. In addition, it has an engraving (1.3-mm deep, filled with white ink) that separates the outermost crystals from the rest of the array. A schematic of the scintillator array together with the photodetector is shown in Fig. 1.

### B. Photodetectors

We measure the scintillation light with an array of digital silicon photomultipliers (dSiPMs) from PDPC of the type DPC 3200-22 [18]. This detector consists of 64 pixels, each $3.2 \times 3.88$ mm$^2$ in size and every pixel has 3200 single photon avalanche photodiodes (SPADs) as photosensitive elements. In contrast to conventional SiPMs, these are coupled to individual logic circuits, which charge and read out the photodiodes. To reduce the dark count rate, we deactivate the noisiest 20% of the SPADs, based on a dark count measurement [19]. The photodetector array is self-triggering with a two-level trigger scheme. To pass the first trigger threshold, three photons are required on average. After this first trigger, the validation time window starts, which in the case of a successful validation is followed by the integration window.

We use a validation threshold that requires 15.9 photons on average (setting 0x55) with the collimator setup, resulting in a noise count rate of 4 Hz/mm$^2$ without any scintillator attached. For the PET scanner, we use a higher validation threshold, which requires an average of 27.5 photons (setting 0x54) [20], because the scanner is operated at a 10 °C higher temperature. With these settings, the PET scanner has a noise count rate of 1.3 Hz/mm$^2$. The used settings are summarized in Table II.

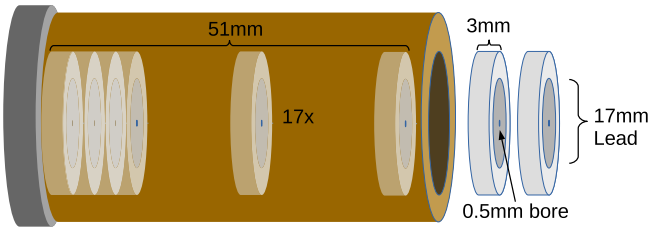


Fig. 2. Schematic of the collimator.

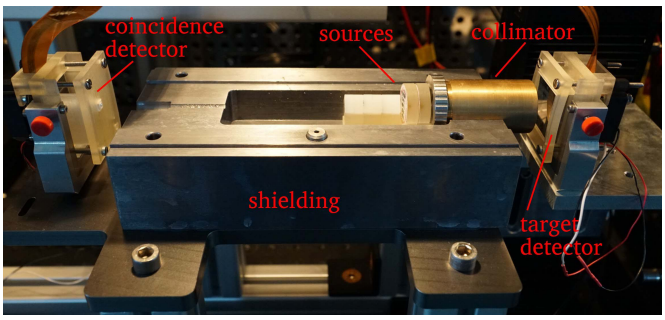


Fig. 3. Image of the experimental setup with opened lead shielding (lower half of the lead block). The coincidence detector is on the left side and the target detector on the right next to the collimator.

### C. Collimator Setup

The collimator setup is used in a configuration with one detector stack and a coincidence detector with a single crystal of $4 \times 4 \times 20$ mm$^3$ directly coupled to one pixel of the digital photodetector. Both photodetectors are read out with the TEK from PDPC. To measure the spatial variation of the detector resolution caused by edge effects and inhomogeneities of the gamma detector, we mount the target detector on an electrically driven two-axis translation stage (LIMES 90, from OWIS, Germany). The manufacturer specifies a maximum positioning repetition error of 2 $\mu$m, and the translation stage has a position feedback system to monitor its movement [21].

The cylindrical collimator is made of 17 slices, each 3-mm thick and with an outer diameter of 25 mm. These slices consist of a lead core with a diameter of 17 mm and a bore diameter of 0.5 mm. The lead core is pressed into a stainless steel ring, and all slices are stacked in a brass tube with an outer diameter of 30 mm. This construction reduces the required aspect ratio of the bore in a single slice to 1:6, while the collimator has a ratio of >1:100. The mechanical misalignment is below 20 $\mu$m, and in the end, this arrangement forms a pinhole collimator with a length of 51 mm. A schematic of the collimator is shown in Fig. 2. The flux of the collimated gamma beam is approximately $10^{-6}$ of the activity placed behind the collimator. To maximize the flux, five $^{22}$Na point sources with a total activity of about 3.5 MBq are aligned along the bore axis behind the collimator. The collimator and the point sources are enclosed by a lead shield to suppress random coincidences and scatter. The backside of the shielding includes a simple bore with a diameter of 4 mm in front of the coincidence detector. An image of the setup is shown in Fig. 3. Furthermore, the whole setup is operated in a light-tight climate chamber, which is cooled to $-16$ °C. This results in a detector temperature of about $-12$ °C and reduces the noise in the photodetectors even further.

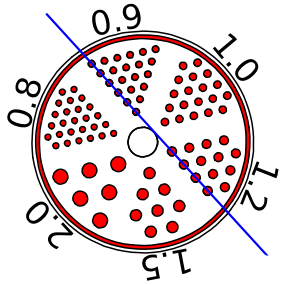


Fig. 4. Sketch of the hotrod phantom with the analyzed line profile drawn in blue. The numbers indicate the rod diameters in millimeters. All red areas are filled with FDG for the measurement.

### D. PET Scanner

To analyze the benefits of our filters on the system level, we use the Hyperion-II$^D$ scanner [7]. The scanner has been designed as a PET-MR insert and has been characterized as fully MR-compatible [22]. It consists of 60 detector stacks that are mounted on a ring of ten singles' detection modules. The axial field of view is 97-mm long, and the crystal-to-crystal distance is 209.6 mm. The detector settings are the same as in the collimator setup with the exception of a higher validation threshold (see Table II). The scanner has a liquid cooling system, which was set to $-5$ °C. At this cooling temperature, the photodetectors operate at a temperature of $(3.3 \pm 1.2)$ °C. The data obtained with the scanner have the same information as the data from the TEK, so that we can apply the same processing algorithm for both measurements. For the study in the scanner, we use a Derenzo phantom with different rod sizes between 0.8 and 2 mm (see Fig. 4). The distance between the centers of the rods is twice their diameter, and the phantom was filled with a $^{18}$fluordesoxyglucose (FDG) solution, which had a start activity of 9 MBq. The phantom has an outer diameter of 30 mm, and the diameters of the different rods are given in the image. The blue line indicates the position of the line profile that will be analyzed to evaluate the image quality.

## III. Methods

### A. Crystal Identification

The detector stacks spread the light of a single gamma interaction over multiple photodetector pixels, which consequently requires a method to identify the crystal with the primary interaction from the measured light distribution. In this paper, we use a center of gravity algorithm with a fixed number of input channels, which are the pixel with the highest photon count (main pixel) and its adjacent pixels. If exactly one of the adjacent corner pixels is missing, we extrapolate this pixel's photon count linearly. The center of gravity is compared with a lookup table generated from a previously obtained floodmap to find the closest matching crystal. Schug *et al.* [23] have published a thorough description of this crystal identification

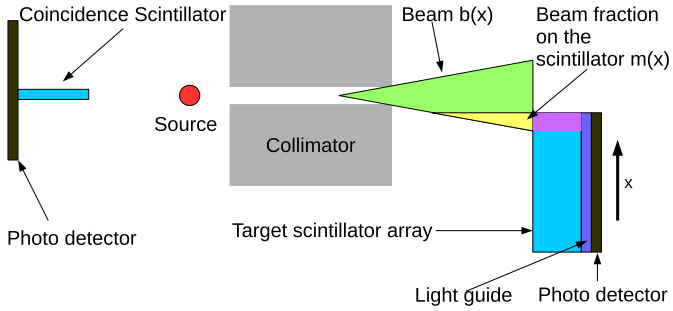


Fig. 5. Schematic of the measurement procedure of the beam profile (not to scale).

algorithm, and the algorithm used and described here is called center of gravity with adaptive corner extrapolation in [23]. For the energy calculation, the pixels around the center of gravity position are used (E-FD; see [23] for details).

Whenever multiple interactions within the same detector stack occur, the outcome of the positioning depends on the distance between the different interactions. If they are close to each other, their light patterns will overlap and the algorithm will identify a crystal between the true positions. In case the interactions are further apart, there will be two or more nonoverlapping light spots on the photo detector. The algorithm will then take the brightest pixel and its neighbors, but ignore all weaker interactions.

### B. Collimator Setup

*1) Beam Profile:* The goal of the collimator setup is to measure the PSF of our pixelated detector with a collimated gamma beam to quantify the quality of our crystal identification algorithm. The measured distribution of identified crystal position for a specific irradiation position of the gamma beam is the convolution of the beam profile and the detector PSF [24]. If the beamwidth is small compared with the detector PSF, the contribution of the beamwidth to the measured distribution is negligible, and therefore this measured distribution can be regarded as a valid approximation of the actual detector PSF.

To measure the profile of the used gamma beam, we measure the coincidence count rate while moving each of the four scintillator edges into the gamma beam in steps of 0.1 mm. Due to the beam's small flux, the measurement time for each irradiation position is 4 h. Fig. 5 illustrates the schematic of the measurement.

To minimize the influence of the data processing, we do not perform any crystal identification and instead use the beam position from the control loop of the translation stage. The only applied filters to acquire the coincidence rate are a photon threshold of 500 measured photons per interaction and a coincidence window of 1.5 ns to minimize noise. For the clustering of DPC hits, a time window of 40 ns is used.

The measured coincidence rates $m(x)$ at the detector position $x$ describe the integral flux across the part of the beam profile that is already irradiating the scintillator. The beam profile $b(x)$ is then the derivative of the measured rate $m(x)$.

TABLE III
FILTERS FOR THE DATA PROCESSING OF THE COLLIMATOR SETUP

| | |
|---|---|
| neighbor cuts | all direct neighbors present |
| energy window | 211 keV-661 keV |
| singles cluster window | 40 ns |
| coincidence window | 1.5 ns |

We have discrete measurement points at the positions $x_i$

$$x_i = x_0 + i \cdot a \tag{1}$$

with a start position $x_0$ and the step width $a$. The discrete derivative of the count rate $m(x)$ is then

$$b_i := b(x_i + a/2) = \frac{m(x_{i+1}) - m(x_i)}{a}. \tag{2}$$

We characterize the beam profile with a Gaussian fit and report the average full-width half-maximum (FWHM) and full-width tenth-maximum (FWTM) of the four measured profiles.

*2) PSF Measurement:* We measure the PSF on a grid of different irradiation positions, which cover the whole scintillator array with a point distance of 1 mm. This grid directly corresponds to the pitch of the scintillator array with an irradiation of each crystal pixel in its center for 30 min, which allows the collection of approximately 6000 events per position. A dedicated noise measurement, where the detector is placed outside of the beam, results in a coincidence rate of 0.15 Hz, which implies a noise contribution of approximately 5% in our PSF measurements. Table III summarizes the parameters and filters used in the analysis.

To calibrate the crystal identification, we obtain the so-called floodmap by filling a histogram with all center of gravity positions from the grid scan. We then fill a lookup table with the positions of the peaks in this floodmaps to map the center of gravity positions to the corresponding pixels [23]. To quantify the spatial resolution from the measured PSFs, we use two different observables. First, we calculate the CIE, which is defined as the ratio of the hits positioned into the irradiated crystal to the total number of hits on the target detector. To describe the tails of the PSF, we use the 90th-percentile diameter, which is the diameter of the circle that encloses 90% of the hits.

The full grid scan contains 900 different data sets with, one for each crystal of the scintillator array, and therefore a total of 900 PSFs and corresponding performance observables. To aggregate all this information, we compare the average values for different filter settings in the following.

### C. Phantom Measurement With PET Scanner

The Hyperion II$^{\mathrm{D}}$ PET scanner is used to measure the activity distribution of a Derenzo hotrod phantom, which is filled with FDG with an activity of 9 MBq. The phantom is placed in the isocenter of the scanner and measured for 762 s. The data of this measurement are processed with the same processing software and settings as the collimator setup (see Table III). In addition, we select only coincidences with exactly two hits and where the second gamma photon interacted with one of the five opposing detectors in the ring (one-to-five coupling).

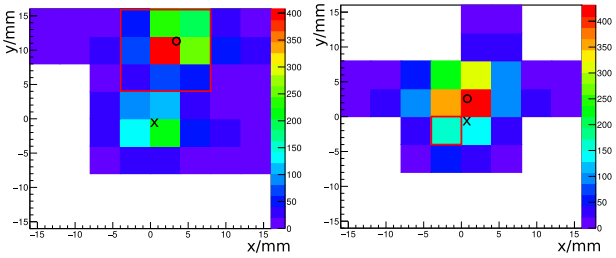


Fig. 6. Example light distributions that are rejected by the second-peak filter (left) or the fifth-brightest-pixel filter (right). The cross in the center indicates the impact point of the beam (known from the collimator position), and the circle marks the position of the identified crystal. In the left plot, the red square surrounds the set of adjacent pixels around the main pixel, and in the right plot, the red square marks the fifth brightest pixel of the light distribution.

Our data acquisition architecture allows the storage of raw photodetector data with subsequent offline data processing with different processing algorithms [25]. The phantom measurements presented here are new data processings of raw data previously used for performance evaluation [26].

The resulting data are reconstructed using a maximum likelihood expectation maximization algorithm including self-normalization and resolution recovery [27] using 32 subset and 16 iterations. The reconstructed 3-D image is projected along the axis of the 20-mm-long rods. Afterward, we analyze a 1-D activity profile along a line through the 0.9- and 1.2-mm rods (see Fig. 4). With this profile, we compute the PtV ratios for each rod and calculate the average PtV ratios for both rod sizes. This data analysis is then repeated with and without the filtering to investigate and quantify its benefits.

### *D. Second-Peak Filter*

The second-peak filter is designed to reject events with multiple gamma interaction, which are far apart from each other.

Fig. 6 shows an example of the measured light distribution of such an event. The filter compares all photon counts of nonadjacent pixels $N_i$ to the photon count of the brightest pixel $N_{\max}$. Then, the filter rejects all events where this ratio is above a certain threshold $t$

$$t < \frac{N_i}{N_{\max}}, \quad i \in \text{Non-adjacent pixels.}$$

In the example in Fig. 6, the nonadjacent pixels $i$ are all the pixels outside the red square around the main pixel. The optimal threshold value $t$ is determined from the measurements of the PSF with the collimator setup by maximizing the CIE and minimizing the 90th-percentile diameter.

### *E. Fifth-Brightest-Pixel Filter*

In our detector stack, there are 16 crystals above every inner pixel of our photo detector (12 for edge pixels). For single interaction events, this always leads to an asymmetric light distribution, because no crystal is positioned exactly over the center of a photodetector pixel. Due to this off-center placement, there are four pixels that are measuring

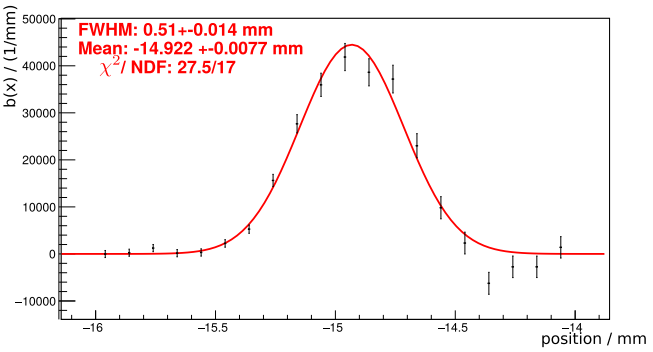


Fig. 7. Example of the measured beam profile (black), with Gaussian fit (red).

significantly more light than all the surrounding pixels: the pixel directly beneath the hit crystal and the three pixels that are the closest to the hit crystal. Thus, for single interactions, the fifth brightest pixel should be significantly darker than the fourth-brightest pixels, since this pixel is further away from the interaction than the other four pixels. If the fifth brightest pixel is brighter than expected, it is very likely that the gamma ray interacted multiple times in the scintillator array, causing overlapping light patterns and therefore an excess of light on this pixel. For the resulting filter, we calculate the ratio of the photon counts of the fifth brightest pixel $N_{5\text{th}}$ compared with the brightest pixel $N_{\max}$ and we will reject events, if this ratio is above a certain threshold $t'$

$$t' < \frac{N_{5\text{th}}}{N_{\max}}.$$

Again, this threshold value $t'$ is optimized by maximizing the CIE and minimizing the 90th-percentile diameter of the measured PSF. Fig. 6 shows the measured light pattern of an event with multiple interactions that are close to each other and would be rejected by this filter. The fifth brightest pixel is marked by a red square.

### *F. Combination of Both Filters*

Although both filters are supposed to reject different classes of events, in practice, the filters and their threshold parameters will likely show some correlation. Therefore, we also optimize the two filter thresholds in the 2-D parameter space. We search for the optimum in this parameter space by performing a grid scan between 0.18 and 0.3 for the threshold of the second-peak filter and between 0.23 and 0.35 for the fifth-brightest-pixel filter. This optimum is used as a strict filter, resulting in the best spatial resolution. We also investigate a set of more loose filter thresholds, which should yield a higher sensitivity with a still decent gain in spatial resolution. In addition, we analyze the relative changes in sensitivity of our detector in dependence of the filter thresholds by plotting the fraction of accepted events.

## IV. Results

### *A. Beam Profile*

An example of the measured beam profile $b(x)$ for one edge of the detector is shown in Fig. 7. The measurement

TABLE IV
MEASURED BEAMWIDTH, AVERAGED OVER ALL FOUR EDGES

| | |
|---|---|
| FWHM | $(0.500 \pm 0.006)$ mm |
| FWTM | $(0.911 \pm 0.011)$ mm |

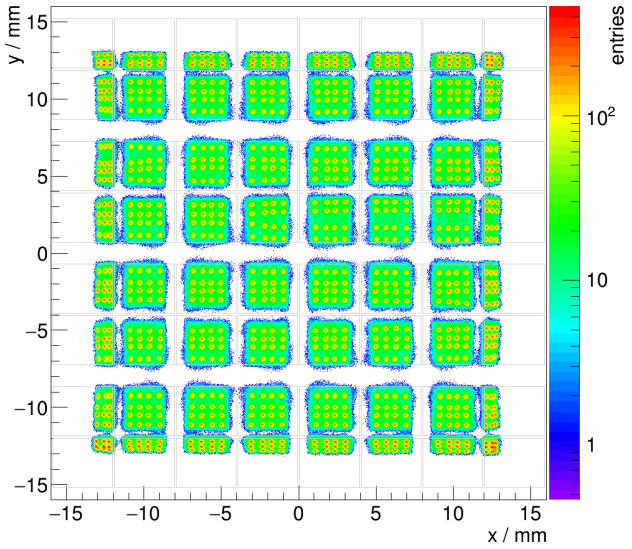


Fig. 8. Floodmap of the center of gravity positions on the target crystal array.

uncertainties in the beam profile increase when detector is moved inside the beam and the measured count rates increase. The Gaussian model describes the beam profile fairly well with a $\chi^2$/NDF value of about 1.6. The average width of the beam profile is shown in Table IV.

### B. Collimator Setup

The floodmap of the target crystal array is shown in Fig. 8. All 900 crystals can be separated clearly, but the space between the different points is smaller at the edges of the crystal array. Especially, the two points in the bottom left and bottom right tend to overlap. The lookup table that is used for the crystal identification is based on this floodmap.

An example histogram of a measured 2-D hit distribution for one impact position is shown in Fig. 9. Each bin in the 2-D histogram represents a crystal of the scintillator array. We analyze the CIE and the 90th-percentile diameter to characterize this distribution. In this example, 54.2% of the incident hits are assigned to the correct crystal, which is the crystal directly beneath the black circle. The rest is scattered across the scintillator array, but a prominent accumulation (radius ~3 mm) around the impact point can be seen. This analysis is repeated for each crystal, and the measured spatial distribution of the CIE is shown in Fig. 10.

The average CIE is 60.0% and varies between 50% and 76%. In the central area, the values vary around 55% and they increase to the edges and corners of the scintillator array. Fig. 11 shows the spatial distribution of the 90th-percentile diameters for the whole scintillator. The 90th-percentile diameter is larger in the center region than

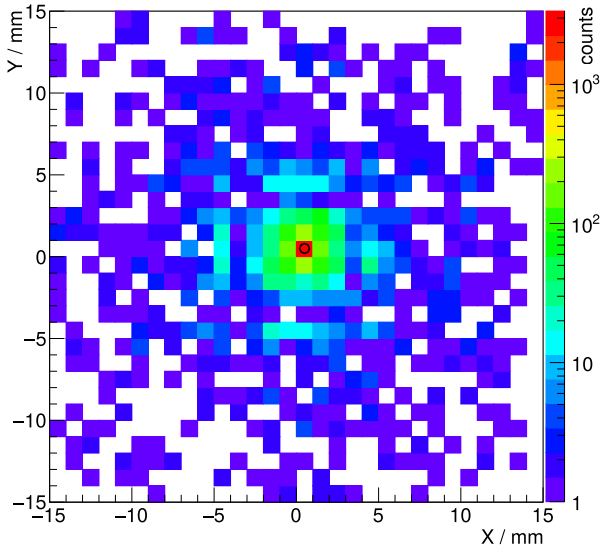


Fig. 9. Example histogram for a measured PSF. The impact point of the beam is marked with the little black circle.

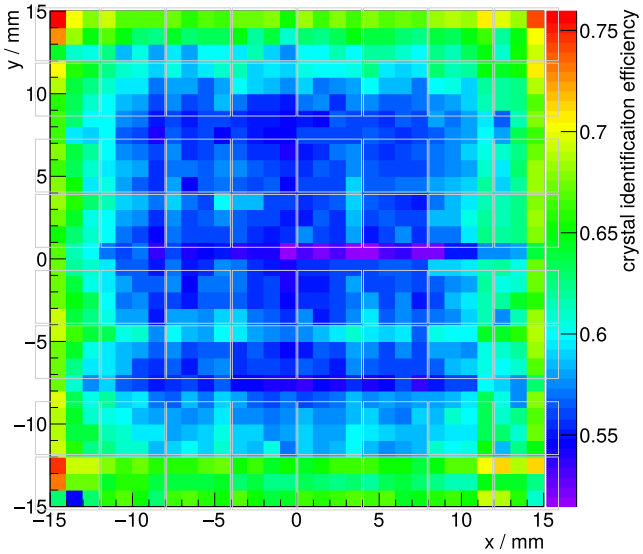


Fig. 10. Spatial distribution of the fraction of correctly identified crystals (CIE). The average value across all bins is 60.0%.

in the outer region. In addition, the 90th-percentile diameter increases over the bonding gaps of the photodetector, where the spatial resolution of the detector is worse. The average value across the whole crystal array is 7.88 mm.

### C. Second-Peak Filter

The results for the optimization of the second-peak filter are shown in Fig. 12. The 90th-percentile diameter and the CIE reach an optimum for a threshold value of 0.18, and at this point, 20.5% of the events are rejected. The filter improves the CIE from 60% to 66.7% and the 90th-percentile diameter from 7.88 to 4.35 mm.

### D. Fifth-Brightest-Pixel Filter

The results for the optimization of the fifth-brightest-pixel filter are shown in Fig. 13. Like for the second-peak fil-

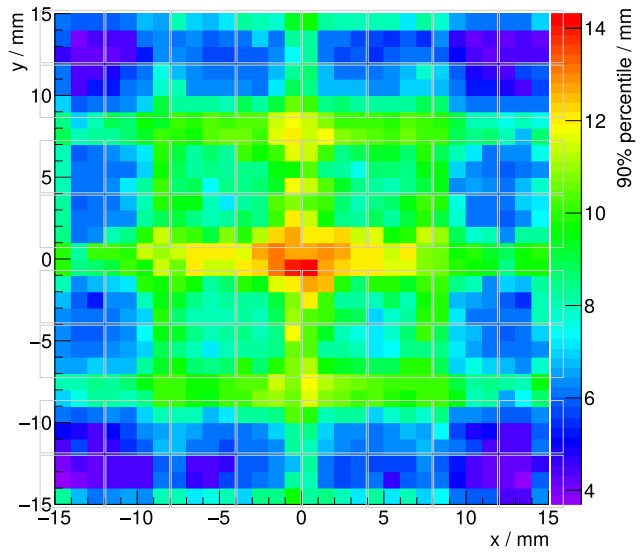


Fig. 11. Spatial distribution of the 90th-percentile diameter values for the whole scintillator. The average value across all bins is 7.88 mm.

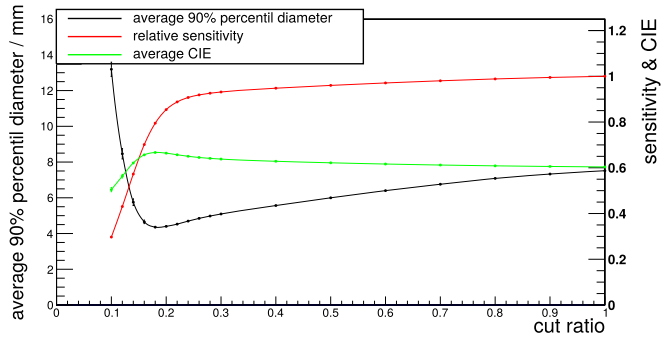


Fig. 12. Impact of different second-peak filter cuts on the average CIE, the average 90th-percentile diameter, and the sensitivity.

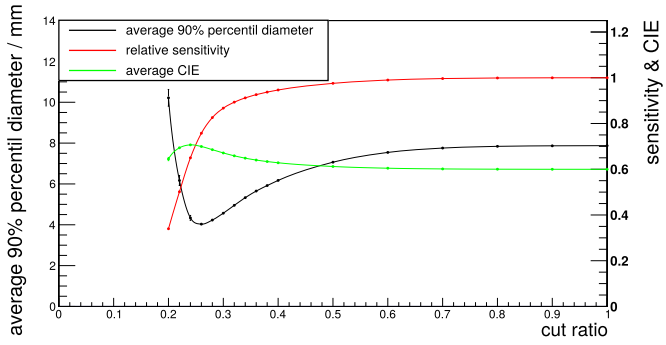


Fig. 13. Impact of different fifth pixel filter cuts on the average CIE, the average 90th-percentile diameter, and the sensitivity.

ter, both observables have a unique optimum, but this time for a threshold value of about 0.26 with a rejection quota of 24.3%. This improves the CIE from 60.0% to 70.0% and the 90th percentile diameter from 7.88 to 4.03 mm.

### *E. Combination of Both Filters*

Based on the analysis of the individual filters, the areas around the optimal threshold values were selected for this

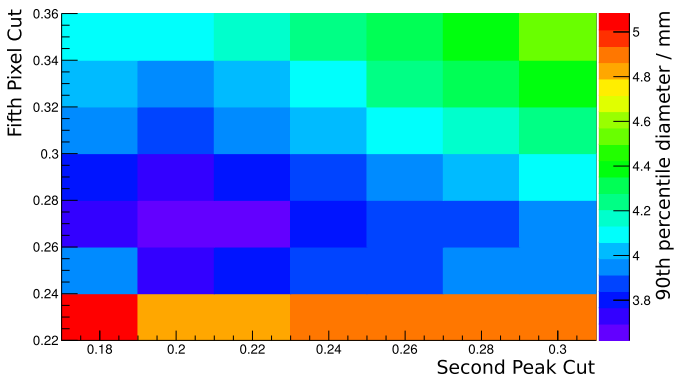


Fig. 14. 90th-percentile diameter as a function of the two filter thresholds.

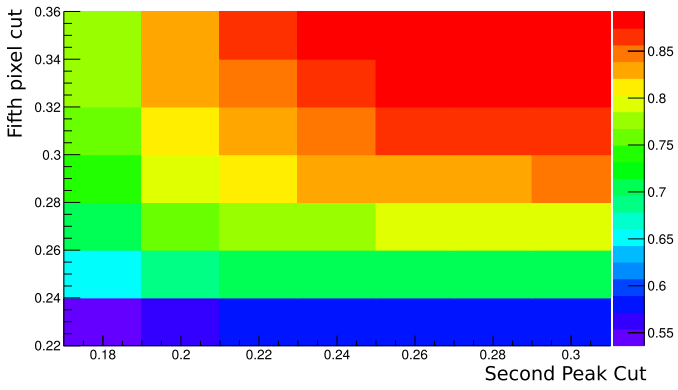


Fig. 15. Relative sensitivity as a function of the two filter thresholds.

TABLE V
EMPIRICAL FILTER THRESHOLD RATIOS

| | Second Peak | Fifth Pixel |
|---|---|---|
| strict | 0.20 | 0.25 |
| loose | 0.25 | 0.30 |

2-D analysis. The average 90th-percentile diameters in dependence of the two thresholds are shown in Fig. 14 and the corresponding plot of the fraction of rejected events in Fig. 15. The average 90th-percentile diameter has a minimum for a second-peak threshold of about 0.20–0.22 and a fifth-brightest-pixel threshold of about 0.25. These are the same thresholds as for the individual cuts, and the analysis of the CIE shows the same behavior.

Fig. 15 shows the relative sensitivity in dependence of the threshold values of the two filters. The relative sensitivity is nearly constant at about 85% for the top right area of the plot. It drops to its minimum of about 55% in the bottom left corner. Based on these results, the two filter settings are selected according to Table V.

The strict setting is placed at the position of the smallest 90th-percentile diameter, while the loose setting is placed at the edge of the large 85% region in the sensitivity plot. The results for the two selected filter settings are summarized in Table VI. For comparison, we performed the same analysis with different energy windows as shown in Table VI.

TABLE VI
RESULT SUMMARY

| cut | # coinc | sensitivity | ∅ CIE | 90th-percentile |
|---|---|---|---|---|
| Wide energy window of 211 keV-661 keV | | | | |
| no | 5.42 m | 100 % | 60.0 % | 7.88 mm |
| loose | 4.58 m | 84.5 % | 68.3 % | 3.98 mm |
| strict | 3.68 m | 67.9 % | 71.4 % | 3.71 mm |
| Moderate energy window of 311 keV-611 keV | | | | |
| no | 3.84 m | 70.8 % | 60.4 % | 6.78 mm |
| loose | 3.29 m | 60.7 % | 68.5 % | 3.70 mm |
| strict | 2.63 m | 48.5 % | 71.9 % | 3.24 mm |
| Narrow energy window of 411 keV-561 keV | | | | |
| no | 2.70 m | 49.8 % | 63.6 % | 5.00 mm |
| loose | 2.41 m | 44.5 % | 70.0 % | 3.28 mm |
| strict | 1.92 m | 35.4 % | 73.2 % | 2.81 mm |

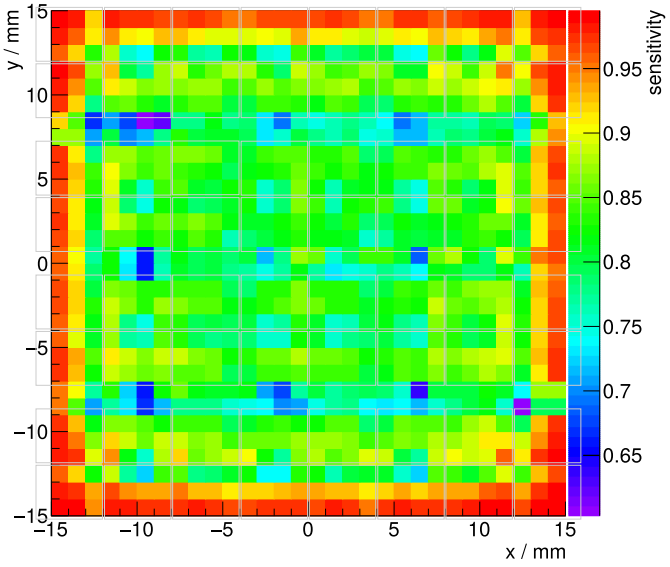


Fig. 16. Relative sensitivity after the filtering with the loose setting. The pixels of the dSiPMs are marked with gray squares.

Finally, we analyzed the relative sensitivity in dependence of the crystal position on the scintillation array while applying the loose filter. The corresponding plot is shown in Fig. 16. The sensitivity is relatively constant in the central part of the detector stack with values around 80%. Above the bond gaps of the chip, the sensitivity drops slightly, and in the outermost crystal row, it increases to nearly 1.

### F. Filtering on the System Level

To analyze the impact of the filters on the system level, we analyzed the PET data of the Derenzo hotrod phantom. The reconstructed images of the activity distribution are shown in Fig. 17, one without filtering and the other with the loose filter applied. The gray and black areas of no activity in the phantom are visibly darker after filtering, resulting in a bigger contrast of the hot rods. To quantify this improvement, we look at the line profiles plotted in Fig. 18. In the profile, one can clearly see that our filters remove background noise from the image, because all the valleys of the profile with

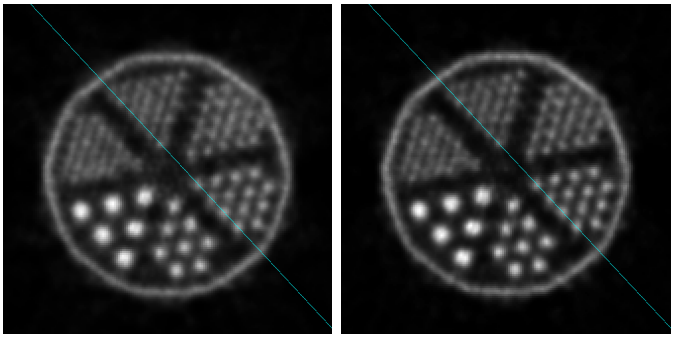

Fig. 17. Reconstructed phantom data, without (left) and with (right) filtering.

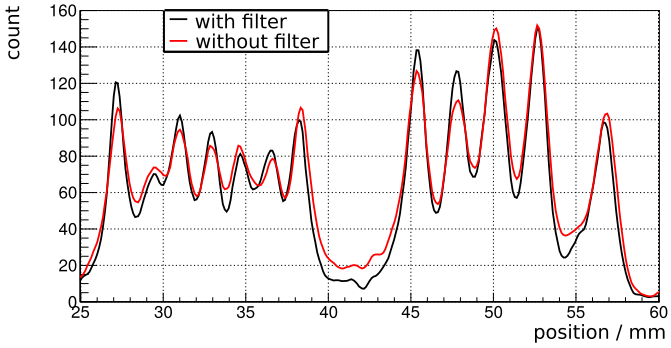


Fig. 18. Profile of the hotrod phantom.

TABLE VII
RESULTS OF THE PHANTOM MEASUREMENT

| cut | # coinc | ∅ PtV ratio 1.2 | ∅ PtV ratio 0.9 |
|---|---|---|---|
| no cut | 160 mil. | 2.10 ± 0.13 | 1.42 ± 0.11 |
| loose cut | 109 mil. | 2.47 ± 0.15 | 1.54 ± 0.11 |
| ratio | 68 % | 118 % | 108 % |

filtering are below the ones without filtering. The resulting PtV ratios for two selected rod sizes are stated in Table VII. For this PET scan, we reject 32% of the coincidences, while improving the PtV ratios by 18% for the larger rods and by 8% for the smaller rods.

## V. DISCUSSION

### A. Beam Profile

The presented method to measure the beam profile works well, but takes about five days of measurement time per edge on our setup in combination with a 3.5-MBq source. The increase in the profile uncertainty is caused by the increase in count rates when the detector is moved into the beam. These increased count rates result in an increase in the absolute Poissonian uncertainties. The data points in the beam profile are proportional to the change in count rate, and therefore the profile uncertainty is proportional to the absolute uncertainties of the count rates. The measured beamwidth of 0.50-mm FWHM and 0.9-mm FWTM (Table IV) is sufficiently narrower than the crystal pitch of the array (1 mm) so that the majority of gamma photons first interact with the

irradiated crystal. This allows us to neglect the contribution of the beamwidth to the measured detector hit distribution.

### *B. Collimator Setup*

The example PSF in Fig. 9 illustrates that about 45% of the hits are positioned to other crystals than the irradiated one. The events in the tails of the PSF are predominantly mispositioned due to intercrystal Compton scatter. Measuring the PSF directly with a collimated gamma beam allows comparison with similar measurements performed with monolithic scintillators, which observe similar tails of their PSFs [15], [28].

The average 90th-percentile diameter is an observable, which depends mainly on the tails of the PSF and is therefore strongly influenced by the fraction of intercrystal scatter. With our unfiltered center of gravity algorithm, we measure an average 90th-percentile diameter of 7.9 mm, which is significantly larger than the reported 90th-percentile of monolithic detectors of approximately 5.2 mm [15]. This suggests that the spatial resolution of a center of gravity algorithm is strongly degraded by intercrystal scatter than the spatial resolution of the $k$-nearest-neighbor algorithm, used in [15].

The 90th-percentile is also much stronger improved by a narrower energy window than the CIE, which gives more support to the hypothesis that the tails of the PSF mainly consist of hits with intercrystal scatter. Therefore, we expect and observe that an effective scatter filter will have the biggest effect on the 90th-percentile and we believe that this value is a descriptive observable for the influence of scatter on the spatial resolution. In addition, this value is independent of the crystal pixel size as long as the crystal pitch is significantly smaller than the 90th-percentile diameter. The CIE on the other hand strongly depends on the size of the crystal pitch, as larger crystals will naturally increase the CIE. Nevertheless, the CIE is still a valuable and simple observable to describe the central part of the PSF and to compare different data processing algorithms on the same detector.

Alternative common observables such as the FWHM of the PSF degrade to the size of the crystal pitch for a sufficiently high CIE with a naive definition of the FWHM. Therefore, such observables would not provide any information on the quality beyond a certain CIE threshold, which is easily reached with the detectors used in this paper. More complex definitions of the FWHM, which, for example, determine the maximum using a fit and determine the position of half the maximum with interpolation, mainly depend on the ratio of the counts in the irradiated pixel and the neighboring pixels. As another possible FWHM definition, one could fit a Gaussian distribution to the central part of the PSF and then determine the FWHM from the Gaussian's $\sigma$. However, such a definition strongly depends on the chosen fit range, because of the influence of the non-Gaussian tails. In addition, such nontrivial definitions of the FWHM prevent meaningful comparisons with FWHM results of other groups, since a commonly established FWHM definition in the community is lacking. In conclusion, we find that the two observables used in this paper are simple, robust, and orthogonal, with the CIE describing the central part of the PSF and the 90th-percentile describing the tails.

The large tails and high 90th-percentile diameters of the PSF suggest the potential for improvements of the spatial resolution by rejecting events with intercrystal scatter. This leads us to the development of the described filters and demonstrates the potential of the here described collimator setup as a tool to directly evaluate the spatial resolution of a detector.

Both observables result in similar optimal threshold values, suggesting that we reach an optimal spatial resolution for both the central parts and the tails of the PSF. The 2-D optimization of both filters also simultaneously finds a similar optimum. However, this optimum appears to be relatively broad, as moving to more loose thresholds only slightly degrades the spatial resolution. On the other hand, the relative sensitivity decreases more sharply for stricter thresholds. Therefore, we chose a set of loose threshold values that have an almost optimal spatial resolution and a significantly higher sensitivity than the optimal set of threshold values for application of the filter on the PET scanner data.

The comparison of our filter with a narrow energy filter in Table VI shows that our filters achieve better spatial resolution while preserving a higher sensitivity. Our filter is therefore both a more efficient and effective filter for intercrystal scatter than an energy filter and should be the preferred solution for small-animal scanners with little object scatter.

Both the spatial resolution and the relative sensitivity improve at the edges of the detector stack. This can be explained by the fact that multiple interactions are less likely to occur near the edges of the scintillator array, because the scattered gamma is more likely to escape the scintillator without a second interaction. In addition, the significant increase in the 90th-percentile diameter can also partially be caused by a cutoff of the PSF at the edge of the stack and the consequential removal of the tails. There is a slight degradation in both the spatial resolution and the relative sensitivity over the bond gaps of the detector, where we lose the most intense part of the scintillation light.

### *C. Phantom Measurement With PET Scanner*

The expected sensitivity loss when applying the filters to coincidence detection is the square of the sensitivity loss of a single detector stack. We therefore expect a drop in relative sensitivity of $0.845^2 = 0.714$ when we apply the filters to our PET scan. The measured value is 68.1%, which is slightly below this expectation.

The reconstructed image and the profile line show a decreased noise floor. The decreased noise floor also explains the increased PtV ratios after filtering, since the depth of the valleys is strongly influenced by the amount of noise. This decrease in noise fits very well to the significantly reduced tails of the PSF of the filtered data, which are the events with a large positioning error.

A positive side effect of the filtering is a significant reduction in processing time. The required time for the iterative image reconstruction roughly scales with the number of coincidences, so the filters reduce the reconstruction time by about 30%.

Even though the used Derenzo phantom is the de facto standard for evaluation of small-animal PET performance, its hot rods are embedded in a cold background of polyethylene and are therefore not a realistic application scenario. Unfortunately, a more realistic phantom with very small-structured hot rods in a warm background would be very challenging to manufacture, and thus it is not available on the market. On the other hand, the natural variance in anatomy and metabolism of mice makes the quantitative evaluation of our filters on a real application scenario challenging. We nevertheless intend to apply our filters on future small-animal studies performed with our scanner to investigate their performance for real applications.

## VI. Conclusion

Our collimator setup allows the direct evaluation of the spatial resolution of scintillation detectors. This method is already well established for the calibration and evaluation of monolithic scintillators, but has so far rarely been used for pixelated detectors. This direct measurement of the PSF of the detectors allows a direct comparison with monolithic scintillators and gives a valuable benchmark for the evaluation of different crystal identification algorithms.

We used these data to develop two simple but effective filters to reject intercrystal scatter events based on their measured light distribution. The observed improvements of the measured PSF could also be reproduced on a system level by applying the same filters to the data of a scan obtained with the Hyperion II$^{D}$ PET scanner. By rejecting the identified scatter events, we are able to increase the image quality visibly, while the processing and reconstruction time decreases proportional to the number of rejected events.

Thanks to the simplicity of the presented filters, it will be possible to implement the filters directly into the FPGA of the detector stacks to decrease data rates and storage usage in the future. Furthermore, these filters could even be implemented into a fully analog signal processing chain.

## References


[1] C. S. Levin and E. J. Hoffman, "Calculation of positron range and its effect on the fundamental limit of positron emission tomography system spatial resolution," *Phys. Med. Biol.*, vol. 44, no. 3, p. 781, 1999. [Online]. Available: http://stacks.iop.org/0031-9155/44/i=3/a=019

[2] K. Shibuya *et al.*, "Annihilation photon acollinearity in PET: Volunteer and phantom FDG studies," *Phys. Med. Biol.*, vol. 52, no. 17, p. 5249, 2007. [Online]. Available: http://stacks.iop.org/0031-9155/52/i=17/a=010

[3] J. R. Stickel, J. Qi, and S. R. Cherry, "Fabrication and characterization of a 0.5-mm lutetium oxyorthosilicate detector array for high-resolution PET applications," *J. Nucl. Med.*, vol. 48, no. 1, pp. 115–121, 2007.

[4] S. Surti *et al.*, "Imaging performance of a-PET: A small animal PET camera," *IEEE Trans. Med. Imag.*, vol. 24, no. 7, pp. 844–852, Jul. 2005.

[5] C. C. Constantinescu and J. Mukherjee, "Performance evaluation of an Inveon PET preclinical scanner," *Phys. Med. Biol.*, vol. 54, no. 9, p. 2885, 2009. [Online]. Available: http://stacks.iop.org/0031-9155/54/i=9/a=020

[6] M. Bergeron *et al.*, "Performance evaluation of the LabPET APD-based digital PET scanner," *IEEE Trans. Nucl. Sci.*, vol. 56, no. 1, pp. 10–16, Feb. 2009.

[7] B. Weissler *et al.*, "A digital preclinical PET/MRI insert and initial results," *IEEE Trans. Med. Imag.*, vol. 34, no. 11, pp. 2258–2270, Dec. 2015.

[8] Y. Yang and S. R. Cherry, "Observations regarding scatter fraction and NEC measurements for small animal PET," in *Proc. IEEE Nucl. Sci. Symp. Conf. Rec.*, vol. 6. Oct. 2004, pp. 3906–3910.

[9] A. Phunpueok, W. Chewpraditkul, V. Thongpool, and D. Aphairaj. (2012). *Comparison of Photofraction for LuYAP:Ce, LYSO:Ce and BGO Crystals in Gamma Ray Detection*. [Online]. Available: http://www.repository.rmutt.ac.th/xmlui/handle/123456789/1298

[10] Y. Shao, S. R. Cherry, S. Siegel, and R. W. Silverman, "A study of intercrystal scatter in small scintillator arrays designed for high resolution PET imaging," *IEEE Trans. Nucl. Sci.*, vol. 43, no. 3, pp. 1938–1944, Jun. 1996.

[11] N. Zeraatkar, M. R. Ay, S. Sarkar, P. Geramifar, and A. Rahmim, "Quantitative investigation of inter-crystal scatter and penetration in the GE discovery RX PET/CT scanner using Monte Carlo simulations," in *Proc. IEEE Nucl. Sci. Symp. Conf. Rec. (NSS/MIC)*, Oct. 2010, pp. 2403–2408.

[12] S.-J. Park, W. L. Rogers, and N. H. Clinthorne, "Effect of intercrystal compton scatter on efficiency and image noise in small animal PET module," in *Proc. IEEE Nucl. Sci. Symp. Conf. Rec.*, vol. 4. Oct. 2003, pp. 2272–2277.

[13] M. Rafecas, G. Boning, B. J. Pichler, E. Lorenz, M. Schwaiger, and S. I. Ziegler, "Characterization and processing of inter-crystal scatter in a dual layer, high resolution LSO-APD-PET," in *Proc. IEEE Nucl. Sci. Symp. Conf. Rec.*, vol. 2. Nov. 2001, pp. 1128–1132.

[14] N. Gross-Weege, D. Schug, P. Hallen, and V. Schulz, "Maximum likelihood positioning algorithm for high-resolution PET scanners," *Med. Phys.*, vol. 43, no. 6, pp. 3049–3061, 2016.

[15] G. Borghi, V. Tabacchini, and D. R. Schaart, "Towards monolithic scintillator based TOF-PET systems: Practical methods for detector calibration and operation," *Phys. Med. Biol.*, vol. 61, no. 13, pp. 4904–4928, 2016.

[16] S. España, R. Marcinkowski, V. Keereman, S. Vandenberghe, and R. van Holen, "DigiPET: Sub-millimeter spatial resolution small-animal PET imaging using thin monolithic scintillators," *Phys. Med. Biol.*, vol. 59, no. 13, p. 3405, 2014. [Online]. Available: http://stacks.iop.org/0031-9155/59/i=13/a=3405

[17] D. Schug *et al.*, "PET performance and MRI compatibility evaluation of a digital, ToF-capable PET/MRI insert equipped with clinical scintillators," *Phys. Med. Biol.*, vol. 60, no. 18, p. 7045, 2015. [Online]. Available: http://stacks.iop.org/0031-9155/60/i=18/a=7045

[18] C. Degenhardt *et al.*, "The digital silicon photomultiplier—A novel sensor for the detection of scintillation light," in *Proc. IEEE Nucl. Sci. Symp. Conf. Rec. (NSS/MIC)*, Sep. 2009, pp. 2383–2386.

[19] T. Frach, G. Prescher, C. Degenhardt, R. de Gruyter, A. Schmitz, and R. Ballizany, "The digital silicon photomultiplier—Principle of operation and intrinsic detector performance," in *Proc. IEEE Nucl. Sci. Symp. Conf. Rec. (NSS/MIC)*, Oct. 2009, pp. 1959–1965.

[20] *PDPC-TEK User Manual, Philips Digital Photon Counting*, Philips Digital Photon Counting, Aachen, Germany, 2014.

[21] *Linearmesstisch LIMES 90, 41.091.101E*, Owis, Staufen i. Br., Germany, 2008.

[22] J. Wehner *et al.*, "MR-compatibility assessment of the first preclinical PET-MRI insert equipped with digital silicon photomultipliers," *Phys. Med. Biol.*, vol. 60, no. 6, p. 2231, 2015. [Online]. Available: http://stacks.iop.org/0031-9155/60/i=6/a=2231

[23] D. Schug *et al.*, "Data processing for a high resolution preclinical PET detector based on Philips DPC digital SiPMs," *IEEE Trans. Nucl. Sci.*, vol. 62, no. 3, pp. 669–678, Jun. 2015.

[24] M. C. Maas *et al.*, "Monolithic scintillator PET detectors with intrinsic depth-of-interaction correction," *Phys. Med. Biol.*, vol. 54, no. 7, pp. 1893–1908, 2009.

[25] B. Goldschmidt *et al.*, "Software-based real-time acquisition and processing of PET detector raw data," *IEEE Trans. Biomed. Eng.*, vol. 63, no. 2, pp. 316–327, Feb. 2016.

[26] D. Schug *et al.*, "Initial PET performance evaluation of a preclinical insert for PET/MRI with digital SiPM technology," *Phys. Med. Biol.*, vol. 61, no. 7, p. 2851, 2016.

[27] A. Salomon, B. Goldschmidt, R. Botnar, F. Kiessling, and V. Schulz, "A self-normalization reconstruction technique for PET scans using the positron emission data," *IEEE Trans. Med. Imag.*, vol. 31, no. 12, pp. 2234–2240, Dec. 2012.

[28] V. Tabacchini, D. R. Schaart, G. Borghi, and B. J. Peet, "A 32 mm × 32 mm × 22 mm monolithic LYSO:Ce detector with dual-sided digital photon counter readout for ultrahigh-performance TOF-PET and TOF-PET/MRI," *Phys. Med. Biol.*, vol. 61, no. 13, pp. 4929–4949, 2016.